Cloud feedback depends on Southern Ocean salinity

Maofeng Liu[1*], Brian Soden[1], Gabriel Vecchi[2,3], Haozhe He[1], Chenggong Wang[4]

[1]Rosenstiel School of Marine and Atmospheric Science, University of Miami, Miami, FL 33149

[2]Department of Geosciences, Princeton University, Princeton, NJ 08544

[3]High Meadows Environmental Institute, Princeton University, Princeton, NJ 08544

[4]Program in Atmospheric and Oceanic Sciences, Princeton University, Princeton, NJ 08540

*Corresponding author: mxl1744@rsmas.miami.edu; maofengliu2012@gmail.com

Key words: Southern Ocean salinity, cloud feedback, climate sensitivity, climate models

Abstract

The uncertainty in equilibrium climate sensitivity (ECS) has remained persistently unchanged for the past four decades[1–4], with cloud feedback[3,5–11] as a primary source of the uncertainty. Here we show that a key component of this uncertainty is rooted in the impact of base-state Southern Ocean salinity on cloud feedback. Sea surface salinity in the sinking zone of the Southern Ocean (45°-60°S) statistically explains half of the inter-model variance in shortwave cloud feedback from a set of 40 Coupled Model Intercomparison Project Phase 6 climate models. Models with greater salinity in this region sequester more heat in the deep ocean[12], reducing the surface warming in the Southern Ocean. This acts to increase lower tropospheric stability[13] which, combined with reduced surface warming, induce a more negative shortwave cloud feedback[14,15], both locally and over remote tropical and subtropical oceans. This remote impact[16–19] is related to enhanced northward advection of Southern Ocean surface waters associated with the strengthening of the southeasterly trade winds, especially in the Southeastern Pacific, transporting the surface warming differences to subtropical oceans. Using observed surface salinity as an emergent constraint argues against models with a strongly positive cloud feedback and high ECS due to their fresh bias in the Southern Ocean[20]. Our results highlight the potential of improved simulation of cloud feedback through dynamical constraint of climate models with salinity observations.

Main

Reducing the uncertainty in equilibrium climate sensitivity (ECS) has been a long-standing challenge facing the climate modeling community. This uncertainty, roughly 1.5-4.5ºC warming in response to a CO_2 doubling, has remained largely unchanged from the Charney report[1] in 1979 to the present-day Coupled Model Intercomparison Project Phase 6 (CMIP6)[2,3]. At the heart of this uncertainty is the cloud feedback[3,5–11], long recognized to be primarily due to the profound challenge for climate models in simulating clouds, arising from their multi-scale nature and our incomplete understanding of processes[5].

In recent years, it has been well-established that climate sensitivity is not constant but evolves substantially over time[13,17,21–27]. The time-dependent nature of climate sensitivity is strongly determined by the evolving spatial pattern of ocean heat uptake (OHU)[16,17]. Subpolar OHU, primarily in Southern Ocean[18], tends to have a larger OHU efficacy[25] – a higher efficiency in cooling the Earth – than tropical OHU. The OHU impact on time-dependent climate sensitivity is regulated by shortwave (SW) cloud feedback[16–18], consistent with Andrews et al.[28] that the increased climate sensitivity over time is largely attributed to the SW cloud feedback. Building on these previous studies, we further demonstrate that this well-established physical link between OHU, cloud feedback, and climate sensitivity applies not only in the time dimension, but also in models' dimension; that is, the extensive spread in cloud feedback and climate sensitivity among CMIP climate models largely depends on their simulation of Southern Ocean heat uptake. This spread is, in turn, regulated by the spread in models' base-state surface salinity in the Southern Ocean.

Southern Ocean heat uptake is strongly linked to the upper cell of the meridional overturning circulation (MOC)[29]. A recent study[30] on the delayed Southern Ocean warming provides a useful framework: surface waters south of the Antarctic Circumpolar Current (ACC) warmed due to increased greenhouse gas emissions are transported northward by the anomalous Ekman current and sequestrated into ocean interior north of the ACC through transformed sinking water masses[31,32]; this process is sustained by the damping effect in warming by unmodulated deep waters upwelled southward to supply the surface waters.

The importance of ocean stratification in the subduction rate of these surface waters is demonstrated by a recent study[33] applying a stratification index for statistically constraining both heat and carbon uptake in the Southern Ocean from a set of CMIP5&6 earth system models. Ocean salinity, relative to temperature, is a better indicator of the stratification in the Southern ocean due to its dominant role in ocean density for cold waters[20,34]. Extratropical Southern Ocean sea surface salinity (SSS) has been successfully applied for an emergent constraint of Southern Ocean carbon sink in CMIP5&6 earth system models[20]. In addition, the important role of salinity in OHU is highlighted by a recent study[12] – the subtropical salinification due to enhancement in global hydrological cycle plays an important role in enhancing the OHU and moderating climate warming. Based on these studies, we further demonstrate that ocean salinity in the sinking zones is a key player in explaining model differences in Southern Ocean heat uptake. Subsequently, the impact of Southern Ocean heat uptake on the inter-model spread of cloud feedback and climate sensitivity is regulated by ocean salinity.

Statistical link between Southern Ocean salinity and cloud feedback regulated by heat uptake

Consistent with our hypothesis, the long-term global-mean SW cloud feedback in response to abrupt CO2 quadrupling (see Methods) shows a significant anti-correlation with base-state extratropical Southern Ocean SSS from the pre-industrial runs among a suite of CMIP6 coupled climate models (Extended Data Fig. 1 a). The averaged SSS within the zone of 45^{o}-60^{o}S (labelled 45^{o}-60^{o}S SSS hereafter; Extended Data Fig. 1 b) accounts for more than half of the variance of the long-term global-mean SW cloud feedback ($r = -0.74$; $p = 9e-6$) among the models (Fig. 1a). The spatial pattern of correlation (Fig. 1c) further highlights the statistical link between extratropical Southern Ocean SSS and SW cloud feedback in both local extra-tropics and remote tropics and subtropics. It is worth noting that the region of the tropical and subtropical southeastern Pacific Ocean with a significant correlation is also the region with the greatest contribution to the inter-model spread in SW cloud feedback[9]. Given the dominant role of SW cloud feedback in total cloud feedback, the anti-correlation shows a small drop for global-mean total cloud feedback ($r = -0.65$; $p = 3e-4$; Fig. 1b) and its spatial pattern (Fig. 1d), partially due to the positive correlation between salinity and longwave cloud feedback (Extended Data Fig. 2).

We further sort the models based upon base-state 45^{o}-60^{o}S SSS (see Methods) and examine the composite differences between the top and bottom SSS models. Relative to the bottom models, the top 45^{o}-60^{o}S SSS models show a much weaker base-state ocean stratification due to higher upper-level density and lower deep-level density in the Southern Ocean (Fig. 2a), with a dominant contribution from ocean salinity relative to ocean temperature, especially in the 45^{o}-60^{o}S zone (Fig. 2b, c). The weaker ocean stratification is statistically associated with more negative SW cloud feedback, highlighted by the negative (positive) correlation between Southern Ocean density and SW cloud feedback in the upper (relatively deep) oceans (Fig. 2d); stronger correlations are seen in the upper ocean, consistent with its greater contribution to the ocean stratification difference (Fig. 2a). These results suggest that the statistically significant link between 45^{o}-60^{o}S SSS and SW cloud feedback probably reflects the dominant role of upper-ocean salinity in Southern Ocean stratification[20] and further more in OHU[33] and SW cloud feedback[16–18].

We examine the impact of ocean stratification on Southern Ocean heat uptake through the difference in ocean warming between top and bottom models (Fig. 2e-h). The sequestration of the anomalous CO2-induced heating in the Southern Ocean starts around 60^{o}S and peaks around 45^{o}S (Fig. 2e, g), consistent with previous CMIP5 model analyses[29] and the salinity zone defined in this study. In addition, the dominance of upper levels in ocean warming highlights the key role of climatological upper MOC in driving Southern Ocean heat uptake[30,35]. The top 45^{o}-60^{o}S SSS models with a weaker base-state stratification produce a deeper warming in the Southern Ocean than the bottom models – less warming in the upper level and greater warming in the relatively deep level[12] (Fig. 2f). The largest difference in warming is seen in upper oceans north of around 60^{o}S where the correlation between ocean density and SW cloud feedback is the strongest (Fig. 2d), and this difference becomes larger over time (Fig. 2f, h). A possible mechanism amplifying the difference is the positive feedback of salinity on ocean stratification[12]. Ocean warming leads to increased stratification over time (Fig. 2i, k) which, however, is increasingly weaker in top salinity models (Fig. 2j, l) due to the enhancement of deeper ocean warming (Fig. 2f, h) and therefore amplifies the difference in ocean warming. Although the less low cloud cover associated with more negative SW cloud feedback in top salinity models reduces surface OHU by reflecting more solar radiation back to space, the net surface OHU south of 35^{o}S is higher in top models relative to bottom models due to the positive contribution from net longwave radiation and latent heat flux (Extended Data Fig. 3). Subsequently, the surface OHU difference is probably not an important contributing factor to the temporal amplification of deeper ocean warming in the top models.

A recent study[36] proposed the Southern Ocean deep convection related to the lower cell of MOC[37–39] as a primary driver of the inter-model spread in Southern Ocean SW cloud feedback and effective climate sensitivity from a CMIP6 model ensemble. Interestingly, the top 45^{o}-60^{o}S SSS models on average have a weaker stratification south of 60^{o}S primarily driven by upper ocean salinity (Fig. 2a-c) and therefore a stronger base-state deep convection that tends to have a larger decline in response to CO2 forcing[36,39]; the greater reduction of cold water convection tends to cause greater ocean warming at depth and less surface warming south of 60^{o}S[36] (Fig. 2h), suggesting that the impact of 45^{o}-60^{o}S salinity on OHU also reflects the role of Southern Ocean deep convection. By ranking models based on the reduction in lower MOC strength[36] instead of 45^{o}-60^{o}S salinity, the difference in base-state ocean stratification (Extended Data Fig. 4a-c) and the vertical distribution of ocean warming (Extended Data Fig. 4d) south of 60^{o}S is slightly more pronounced.

Global-mean SW cloud feedback shows a much larger scattering against CO2-induced reduction in the strength of lower MOC reduction ($r = -0.52$; $p = 0.004$) than against 45^{o}-60^{o}S SSS ($r = -0.77$; $p = 2e-6$) for the same set of CMIP6 models (Extended Data Fig. 5a, b), suggesting that Southern Ocean deep convection[36] is probably less important than surface water subduction north of ACC on the model ensemble level. Consistently, SW cloud feedback has a stronger correlation with the upper-level density north of ACC than south of it (Fig. 2d). In addition, the deep convection zone around Ross sea and Weddell sea[40] with significant correlation between the reduction in lower MOC strength and base-state SSS in (Extended Data Fig. 5c) shows much weaker correlation between SW cloud feedback and base-state SSS (Extended Data Fig. 1b).

However, the impact of Southern Ocean deep convection on SW cloud feedback could be significant for specific cases. For example, CESM2 and NorESM2-LM model, as highlighted by Gjermundsen et al.[36], show a much larger difference in salinity-dominated base-state ocean stratification south of 60^{o}S (Extended Data Fig. 6a-c) than model ensemble comparison (Extended

Data Fig. 4a-c), which drives a striking difference in the vertical distribution of heating in response to CO2 forcing (Extended Data Fig. 6d). The northward transport of cooler surface waters south of ACC in NorESM2-LM impacts the ocean warming in the sinking water zone.

Physical mechanism linking ocean heat uptake, sea surface warming and cloud feedback

A key remaining question is: how do salinity-driven differences in Southern Ocean heat uptake influence the SW cloud feedback? We propose that this connection arises through the OHU impact on sea surface temperature (SST). It is well established that the spatial evolution of SST, in addition to OHU, is another key determinant in the time-dependence of climate sensitivity[13,23,26–28,41–44]. A recent study[27] argued that the two perspectives are equivalent, that is, the dependence of climate sensitivity on the evolving pattern of OHU is exerted by the OHU impact on SST pattern. Similar to the time dimension, it is hypothesized that this mechanism is also responsible for the *inter-model* spread in SW cloud feedback.

A consequence of the deeper ocean warming in top salinity models relative to bottom models (Fig. 2f, h) is reduced surface warming that amplifies over time (Fig. 3a-c). The surface warming difference is seen not only in the local Southern Ocean, but also in remote subtropical and tropical oceans[18,19,45]. The strengthening of the southeasterly trade winds, especially in the Southeastern Pacific, enhances the northward advection of surface waters and impacts the surface warming difference in tropical oceans. The difference in trade wind strengthening between top and bottom salinity models shows a much smaller magnitude than itself (Extended Data Fig. 7), implying that the difference in the strength of wind-evaporation-SST feedback[46] among models may play a less important role.

The difference in SW cloud feedback between top and bottom models (Extended Data Fig. 8) exhibits a similar spatial pattern to SST, consistent with previous studies identifying SST as a key low-cloud controlling factor[14,15,47]. In addition to SST, the lower tropospheric stability (LTS)[14,48] is another key player. The top salinity models, relative to the bottom models, show a much greater LTS represented by estimated inversion strength (EIS)[49] response normalized by global-mean surface warming[17] in both local extratropical Southern Ocean and remote subtropical Indian and Southeastern Pacific Ocean (Fig. 3d-f). These regions are well co-located with areas with significant correlations between 45°-60°S SSS and SW cloud feedback (Fig. 1). It is worth noting that the less SST increase in the top models contributes to a less decrease in EIS, as highlighted by the similarity in spatial pattern of the two (Fig. 3). For Southeastern Pacific with the greatest difference in SW cloud feedback between top and bottom salinity models, LTS is largely controlled by the difference between local SST and West Pacific convective region due to the strong coupling between tropospheric temperature and SST in convective regions. Subsequently, the enhanced difference in west-to-east SST asymmetry between top and bottom models over time leads to temporally increased difference in inversion strength in Southeastern Pacific (Fig. 3).

Consistent with our results, both SST and EIS were found important factors accounting for the spread in marine low cloud cover from CMIP3&5 climate models[14]. Furthermore, both OHU[17,18] and SST perspective[13,23,26–28,41–44] argued that their impact on time-dependent climate sensitivity is regulated by the temporal evolution of LTS[13]. Specifically, the Southeastern Pacific show a substantial decrease in EIS and therefore low cloud cover over time in response to CO2 forcing[13,18], a primary cause for temporally increasing climate sensitivity. This is also the region with the greatest spread in SW cloud feedback among models (Extended Data Fig. 8). The similarity of the physical mechanism between time and model dimension further supports our hypothesis.

Emergent constraint

Here we use the physically based relation between extratropical Southern Ocean SSS and global-mean SW and total cloud feedback as an emergent constraint on the latter using long-term ocean salinity observations. We use a linear model to construct the relationship between the long-term global-mean cloud feedback in response to abrupt CO_2 quadrupling and 45^{o}-60^{o}S SSS averaged over the period of 1968-2014 from CMIP6 historical experiments (see Methods). We do not use SSS south of 60^{o}S for emergent constraint because the impact of Southern Ocean deep convection is secondary and it is partially accounted for by using SSS in the sinking zone.

For both SW and total cloud feedback, the correlation against historical SSS (Fig. 4a, c) is comparable to pre-industrial SSS (Fig. 1). Three observation-constrained ocean salinity data sets[50–52] averaged over the period of 1968-2014 are applied to the regression model, enabling a tighter constraint on cloud feedback. (Fig. 4b, d). The constrained distribution of cloud feedback after argues against models producing high cloud feedback. For instance, the probability of SW (total) cloud feedback exceeding 1 W m^{-2} K^{-1} drops from 17.9% (15.4%) to 0.1% (1.9%) after the constraint.

In addition to cloud feedback, we further applied an emergent constraint on effective climate sensitivity (ECS)[24] and obtained a narrower range (2.6-3.9^{o}C for the 25-75% prediction interval) than the priors (2.8-4.7^{o}C) (Fig. 4 e, f). Similar to cloud feedback, the SSS-based constraint argues against models producing high ECS due to their fresh biases in the Southern Ocean. CMIP6 models tend to produce higher ECS than the previous version[2,3]; 12 of 40 CMIP6 models in our study produce an ECS exceeding 4.5 K. The higher ECS in CMIP6 relative to CMIP5 was partially attributed to their differences in physical representations of clouds that lead to more positive cloud feedback in CMIP6 models due to decreased extratropical low cloud cover[3].

In addition to cloud parameterization, underestimation of extratropical Southern Ocean salinity in considerable CMIP6 models (Fig. 4) is likely another factor, which needs further investigation.

Summary

Reducing the uncertainty in estimating climate sensitivity in response to increased greenhouse gas emissions is a grand challenge facing the climate community. A primary source of the uncertainty is rooted in how clouds respond to warming. In this study, we propose that the Southern Ocean heat uptake dominated by ocean salinity, in addition to models' difference in physical configurations of cloud microphysics parameterizations[5], is another key factor impacting the inter-model spread in cloud feedback. For a suite of 40 CMIP6 coupled climate models, 45^{o}-60^{o}S SSS statistically accounts for more than half of the variance in SW cloud feedback.

The link between extratropical Southern Ocean SSS and cloud feedback has a profound physical basis that is also responsible for the time dependence of climate sensitivity[16–18]. Models with greater upper-ocean salinity in the sinking zones or deep convection zones of Southern Ocean tend to have a deeper ocean warming and therefore less SST increase, leading to an enhanced stabilization of lower troposphere which, in combination with SST pattern, causes increased low cloud cover and more negative cloud feedback in both local Southern Ocean and remote tropics due to Southern Ocean-tropics teleconnection.

The salinity impact on cloud feedback enables a tighter constraint on cloud feedback based on observational SSS data sets, which argues against models with ECS exceeding 4.5 K. Model experiments by artificially modifying extratropical SSS with observations are needed to further evaluate the high ECS models. In addition, our study highlights the importance of continuous salinity measurements based on both satellites and Argo floats for monitoring future cloud feedback and climate sensitivity by statistical constraining or calibrating dynamical models through salinity assimilation.

Methods

Coupled Model Intercomparison Project Phase 6 (CMIP6) models

We use a suite of 40 CMIP6 coupled climate models focusing on both pre-industrial runs and abrupt-4xCO2 runs in which the atmospheric CO2 concentration is increased abruptly by a factor of four. To account for models' difference in spatial resolution, all model outputs are resampled to the same resolution. Not all variables we use are fully available. Data availability and values of key variables are listed in Extended Data Table 1.

Radiative feedback, ECS and estimated inversion strength

The radiative kernel method[53] is employed to compute the radiative feedbacks. The radiative kernel used in this study is derived from CloudSat/CALIPSO measurements[9,54,55]. The radiative kernel for a feedback variable x is defined as $Kx = \partial R/\partial x$, where R is the net TOA flux and x is an individual radiative state variable. Cloud feedback is further decomposed to longwave and shortwave components. The long-term radiative feedback in response to abrupt CO2 quadrupling is computed as the slope of a linear regression between annual global-mean radiative flux anomalies and corresponding global-mean surface temperature anomalies from the standard 150-year abrupt-4xCO2 experiment.

The equilibrium climate sensitivity (ECS) is approximated as the effective climate sensitivity computed using the Gregory method[24] based on the 150-year abrupt-4xCO2 experiment.

We focus on the 700-hPa estimated inversion strength (EIS)[49] and compute it by employing the climlab package in Python (https://climlab.readthedocs.io/en/latest/index.html).

Ocean analysis

The difference in ocean density between top and bottom models is computed as follows:

$$\Delta\rho = \rho_{top} - \rho_{bot} \quad (1)$$

Contribution from both salinity ($\Delta\rho_S$) and temperature ($\Delta\rho_T$) to this difference is computed as follows:

$$\Delta\rho_S = \beta\Delta S\rho_{bot} - \rho_{bot} \quad (2)$$

$$\Delta\rho_T = -\alpha\Delta T\rho_{bot} - \rho_{bot} \quad (3)$$

in which ρ_{top} and ρ_{bot} are the ocean density from top and bottom models, respectively, ΔS and ΔT are the difference in ocean salinity and temperature between top and bottom models, respectively, β is the haline contraction coefficient, and α is the thermal expansion coefficient. ρ, α, β are computed using salinity and temperature as inputs based on Thermodynamic Equation of SeaWater 2010 (TEOS-10) standards[56] implemented in a Python package (GSW-Python; https://teos-10.github.io/GSW-Python/).

The reduction in lower MOC strength in response to CO2 forcing is adopted from Gjermundsen et al.[36]. In their study, the strength of lower MOC is defined as the averaged minimum stream function within the zone of 35°-90°S and the depth below 2,000 m. The reduction in lower MOC strength is then computed as the difference between averages of year 121-150 of the abrupt-4×CO2 runs and corresponding model years of pre-industrial runs.

Observation-constrained ocean salinity data

Three ocean salinity data sets for the period of 1968-2014 are used for the emergent constraint of cloud feedback and ECS: Japan Meteorological Agency (JMA), Japan (labelled Ishii data[50]), Institute of Atmospheric Physics (IAP), China (labelled IAP data[51]), and Ocean Reanalysis System 4 (ORAS4) (labelled ORAS4 data[52]).

Bootstrap method

To reduce the impact of individual models on the results, a bootstrap method is used for all analyses in this study. First, all models are treated equally. A certain number of models are uniformly drawn (with replacement) from all available models. Second, for correlation analysis, the selected model samples are used to compute correlation coefficient and p-value. For model composite analyses, we rank the selected models based upon 45°-60°S SSS, select a collection of models ranked in the top and bottom, respectively, and compute the difference of mean between the two groups. Third, we repeat the second step 10,000 times and compute the mean of difference from the obtained 10,000 samples.

For the analyses with all 40 models available, 30 models are drawn each time and top and bottom 10 models are selected for composite analyses. For surface energy flux analysis, 38 models are available, 30 models are drawn each time, and top and bottom 10 models are selected. For ocean analysis, 34 (25 for MOC) models available, 27 (20) models are drawn each time and top and bottom 9 (7) models are selected. For surface wind analysis, 29 models available, 20 models are drawn each time and top and bottom 7 models are selected. See Extended Data Table 1 for more details.

Emergent constraint

We conducted an ordinary least squares regression between long-term cloud feedback from the abrupt-4xCO2 experiments and 45°-60°S SSS averaged within the period of 1968–2014 from the CMIP6 historical experiments among 39 CMIP6 models. GISS-E2-2-G model is excluded due to the lack of historical SSS variable. The bootstrap method described above is used to draw 30 model samples (with replacement) from pairs of cloud feedback and SSS. The selected samples are used to conduct linear regression. We repeat this process 10,000 times and obtain 10,000 samples of slope and intercept representing their uncertainty. For each pair of slope and intercept, we computed the standard deviation of the residual (assumed to follow Gaussian distribution) and used it to generate 100 residual samples. Subsequently, we can generate one million samples of cloud feedback for each given SSS.

We then apply SSS from the three observational data sets in the bootstrap-based regression, respectively to compute the constrained cloud feedback. Cloud feedback samples estimated from the three data sets were put together to form the final sample space. Finally, we applied the Gaussian kernel to estimate the probability density function for both unstrained and constrained cloud feedback (Fig. 4).

We repeat the whole process for the emergent constraint of ECS.

Author Contribution: M.L., B.S., and G.V. designed the research with input from H.H.; M.L., and H.H. performed analysis with input from W.C.; M.L. wrote the draft; and all the authors contributed to the interpretation of the results and the writing of the paper.

Materials & Correspondence: Correspondence and material requests to Maofeng Liu.

Competing Interest Statement: The authors declare no competing interests.

Data and code availability

The CMIP6 climate model outputs are available at https://esgf-node.llnl.gov/search/cmip6/. The JMA data is available at https://climate.mri-jma.go.jp/pub/ocean/ts/v7.3/. The IAP data is available at http://159.226.119.60/cheng/. The ORAS4 data is available at ftp://ftp-icdc.cen.uni-hamburg.de/EASYInit/ORA-S4/.

The codes will be available in a persistent repository upon acceptance.

Acknowledgements

This work was supported by Award 80NSSC20K0879 from the National Aeronautics and Space Administration and Award DE-SC0021333 from the United States Department of Energy.

Reference

1. Charney, J. G. *et al.* Carbon dioxide and climate: a scientific assessment. (1979).
2. Meehl, G. A. *et al.* Context for interpreting equilibrium climate sensitivity and transient climate response from the CMIP6 Earth system models. *Sci. Adv.* **6**, 1–11 (2020).
3. Zelinka, M. D. *et al.* Causes of Higher Climate Sensitivity in CMIP6 Models. *Geophys. Res. Lett.* **47**, 1–12 (2020).
4. Knutti, R., Rugenstein, M. A. A. & Hegerl, G. C. Beyond equilibrium climate sensitivity. *Nat. Geosci.* **10**, 727–736 (2017).
5. Ceppi, P., Brient, F., Zelinka, M. D. & Hartmann, D. L. Cloud feedback mechanisms and their representation in global climate models. *WIREs Clim. Chang.* **8**, e465 (2017).
6. Caldwell, P. M., Zelinka, M. D., Taylor, K. E. & Marvel, K. Quantifying the Sources of Intermodel Spread in Equilibrium Climate Sensitivity. *J. Clim.* **29**, 513–524 (2016).
7. Webb, M. J., Lambert, F. H. & Gregory, J. M. Origins of differences in climate sensitivity, forcing and feedback in climate models. *Clim. Dyn.* **40**, 677–707 (2013).
8. Bony, S. & Dufresne, J.-L. Marine boundary layer clouds at the heart of tropical cloud feedback uncertainties in climate models. *Geophys. Res. Lett.* **32**, (2005).
9. He, H., Kramer, R. J. & Soden, B. J. Evaluating Observational Constraints on Intermodel Spread in Cloud, Temperature, and Humidity Feedbacks. *Geophys. Res. Lett.* **48**, e2020GL092309 (2021).
10. Soden, B. J. & Held, I. M. An assessment of climate feedbacks in coupled ocean-atmosphere models. *J. Clim.* **19**, 3354–3360 (2006).
11. Dufresne, J.-L. & Bony, S. An Assessment of the Primary Sources of Spread of Global Warming Estimates from Coupled Atmosphere–Ocean Models. *J. Clim.* **21**, 5135–5144 (2008).
12. Liu, M., Vecchi, G., Soden, B., Yang, W. & Zhang, B. Enhanced hydrological cycle increases ocean heat uptake and moderates transient climate change. *Nat. Clim. Chang.* (2021). doi:10.1038/s41558-021-01152-0
13. Ceppi, P. & Gregory, J. M. Relationship of tropospheric stability to climate sensitivity and Earth's observed radiation budget. *Proc. Natl. Acad. Sci.* **114**, 13126 LP – 13131 (2017).
14. Qu, X., Hall, A., Klein, S. A. & Caldwell, P. M. On the spread of changes in marine low cloud cover in climate model simulations of the 21st century. *Clim. Dyn.* **42**, 2603–2626 (2014).
15. Qu, X., Hall, A., Klein, S. A. & DeAngelis, A. M. Positive tropical marine low-cloud cover feedback inferred from cloud-controlling factors. *Geophys. Res. Lett.* **42**, 7767–7775 (2015).
16. Rose, B. E. J., Armour, K. C., Battisti, D. S., Feldl, N. & Koll, D. D. B. The dependence of transient climate sensitivity and radiative feedbacks on the spatial pattern of ocean heat uptake. *Geophys. Res. Lett.* **41**, 1071–1078 (2014).
17. Rose, B. E. J. & Rayborn, L. The Effects of Ocean Heat Uptake on Transient Climate Sensitivity. *Curr. Clim. Chang. Reports* **2**, 190–201 (2016).
18. Lin, Y.-J., Hwang, Y.-T., Lu, J., Liu, F. & Rose, B. E. J. The Dominant Contribution of Southern Ocean Heat Uptake to Time-Evolving Radiative Feedback in CESM. *Geophys. Res. Lett.* **48**, e2021GL093302 (2021).
19. Zhang, X., Deser, C. & Sun, L. Is There a Tropical Response to Recent Observed Southern Ocean Cooling? *Geophys. Res. Lett.* **48**, e2020GL091235 (2021).
20. Terhaar, J., Frölicher, T. L. & Joos, F. Southern Ocean anthropogenic carbon sink

constrained by sea surface salinity. *Sci. Adv.* **7**, eabd5964 (2021).
21. Senior, C. A. & Mitchell, J. F. B. The time-dependence of climate sensitivity. *Geophys. Res. Lett.* **27**, 2685–2688 (2000).
22. Williams, K. D., Ingram, W. J. & Gregory, J. M. Time Variation of Effective Climate Sensitivity in GCMs. *J. Clim.* **21**, 5076–5090 (2008).
23. Gregory, J. M. & Andrews, T. Variation in climate sensitivity and feedback parameters during the historical period. *Geophys. Res. Lett.* **43**, 3911–3920 (2016).
24. Gregory, J. M. *et al.* A new method for diagnosing radiative forcing and climate sensitivity. *Geophys. Res. Lett.* **31**, 2–5 (2004).
25. Winton, M., Takahashi, K. & Held, I. M. Importance of Ocean Heat Uptake Efficacy to Transient Climate Change. *J. Clim.* **23**, 2333–2344 (2010).
26. Armour, K. C., Bitz, C. M. & Roe, G. H. Time-Varying Climate Sensitivity from Regional Feedbacks. *J. Clim.* **26**, 4518–4534 (2013).
27. Haugstad, A. D., Armour, K. C., Battisti, D. S. & Rose, B. E. J. Relative roles of surface temperature and climate forcing patterns in the inconstancy of radiative feedbacks. *Geophys. Res. Lett.* **44**, 7455–7463 (2017).
28. Andrews, T., Gregory, J. M. & Webb, M. J. The Dependence of Radiative Forcing and Feedback on Evolving Patterns of Surface Temperature Change in Climate Models. *J. Clim.* **28**, 1630–1648 (2015).
29. Liu, W., Lu, J., Xie, S.-P. & Fedorov, A. Southern Ocean Heat Uptake, Redistribution, and Storage in a Warming Climate: The Role of Meridional Overturning Circulation. *J. Clim.* **31**, 4727–4743
30. Armour, K. C., Marshall, J., Scott, J. R., Donohoe, A. & Newsom, E. R. Southern Ocean warming delayed by circumpolar upwelling and equatorward transport. *Nat. Geosci.* **9**, 549–554 (2016).
31. Talley, L. D. Closure of the global overturning circulation through the Indian, Pacific, and Southern Oceans: Schematics and transports. *Oceanography* **26**, 80–97 (2013).
32. Sallée, J.-B. *et al.* Assessment of Southern Ocean water mass circulation and characteristics in CMIP5 models: Historical bias and forcing response. *J. Geophys. Res. Ocean.* **118**, 1830–1844 (2013).
33. Bourgeois, T., Goris, N., Schwinger, J. & Tjiputra, J. F. Stratification constrains future heat and carbon uptake in the Southern Ocean between 30°S and 55°S. *Nat. Commun.* **13**, 340 (2022).
34. Downes, S. M., Bindoff, N. L. & Rintoul, S. R. Impacts of Climate Change on the Subduction of Mode and Intermediate Water Masses in the Southern Ocean. *J. Clim.* **22**, 3289–3302 (2009).
35. Morrison, A. K., Griffies, S. M., Winton, M., Anderson, W. G. & Sarmiento, J. L. Mechanisms of Southern Ocean Heat Uptake and Transport in a Global Eddying Climate Model. *J. Clim.* **29**, 2059–2075
36. Gjermundsen, A. *et al.* Shutdown of Southern Ocean convection controls long-term greenhouse gas-induced warming. *Nat. Geosci.* **14**, 724–731 (2021).
37. Gregory, J. M. Vertical heat transports in the ocean and their effect on time-dependent climate change. *Clim. Dyn.* **16**, 501–515 (2000).
38. Marshall, J. & Speer, K. Closure of the meridional overturning circulation through Southern Ocean upwelling. *Nat. Geosci.* **5**, 171–180 (2012).
39. Zhang, L., Delworth, T. L., Cooke, W. & Yang, X. Natural variability of Southern Ocean

convection as a driver of observed climate trends. *Nat. Clim. Chang.* **9**, 59–65 (2019).
40. Zhang, L. & Delworth, T. L. Impact of the Antarctic bottom water formation on the Weddell Gyre and its northward propagation characteristics in GFDL CM2.1 model. *J. Geophys. Res. Ocean.* **121**, 5825–5846 (2016).
41. Andrews, T. *et al.* Accounting for Changing Temperature Patterns Increases Historical Estimates of Climate Sensitivity. *Geophys. Res. Lett.* **45**, 8490–8499 (2018).
42. Stevens, B., Sherwood, S. C., Bony, S. & Webb, M. J. Prospects for narrowing bounds on Earth's equilibrium climate sensitivity. *Earth's Futur.* **4**, 512–522 (2016).
43. Dong, Y., Proistosescu, C., Armour, K. C. & Battisti, D. S. Attributing Historical and Future Evolution of Radiative Feedbacks to Regional Warming Patterns using a Green?s Function Approach: The Preeminence of the Western Pacific. *J. Clim.* **32**, 5471–5491 (2019).
44. Dong, Y. *et al.* Intermodel Spread in the Pattern Effect and Its Contribution to Climate Sensitivity in CMIP5 and CMIP6 Models. *J. Clim.* **33**, 7755–7775 (2020).
45. Hwang, Y.-T., Xie, S.-P., Deser, C. & Kang, S. M. Connecting tropical climate change with Southern Ocean heat uptake. *Geophys. Res. Lett.* **44**, 9449–9457 (2017).
46. Xie, S.-P. *et al.* Global Warming Pattern Formation: Sea Surface Temperature and Rainfall. *J. Clim.* **23**, 966–986 (2010).
47. Klein, S. A., Hall, A., Norris, J. R. & Pincus, R. Low-Cloud Feedbacks from Cloud-Controlling Factors: A Review. *Surv. Geophys.* **38**, 1307–1329 (2017).
48. Klein, S. A. & Hartmann, D. L. The Seasonal Cycle of Low Stratiform Clouds. *J. Clim.* **6**, 1587–1606 (1993).
49. Wood, R. & Bretherton, C. S. On the Relationship between Stratiform Low Cloud Cover and Lower-Tropospheric Stability. *J. Clim.* **19**, 6425–6432 (2006).
50. Ishii, M. *et al.* Accuracy of Global Upper Ocean Heat Content Estimation Expected from Present Observational Data Sets. *Sola* **13**, 163–167 (2017).
51. Cheng, L. *et al.* Improved estimates of changes in upper ocean salinity and the hydrological cycle. *J. Clim.* **33**, 10357–10381 (2020).
52. Balmaseda, M. A., Mogensen, K. & Weaver, A. T. Evaluation of the ECMWF ocean reanalysis system ORAS4. *Q. J. R. Meteorol. Soc.* (2013). doi:10.1002/qj.2063
53. Soden, B. J. *et al.* Quantifying climate feedbacks using radiative kernels. *J. Clim.* **21**, 3504–3520 (2008).
54. Kramer, R. J., Matus, A. V., Soden, B. J. & L'Ecuyer, T. S. Observation-Based Radiative Kernels From CloudSat/CALIPSO. *J. Geophys. Res. Atmos.* **124**, 5431–5444 (2019).
55. Zhang, B., Kramer, R. J. & Soden, B. J. Radiative feedbacks associated with the Madden–Julian oscillation. *J. Clim.* **32**, 7055–7065 (2019).
56. Feistel, R. A Gibbs function for seawater thermodynamics for −6 to 80°C and salinity up to 120gkg–1. *Deep Sea Res. Part I Oceanogr. Res. Pap.* **55**, 1639–1671 (2008).

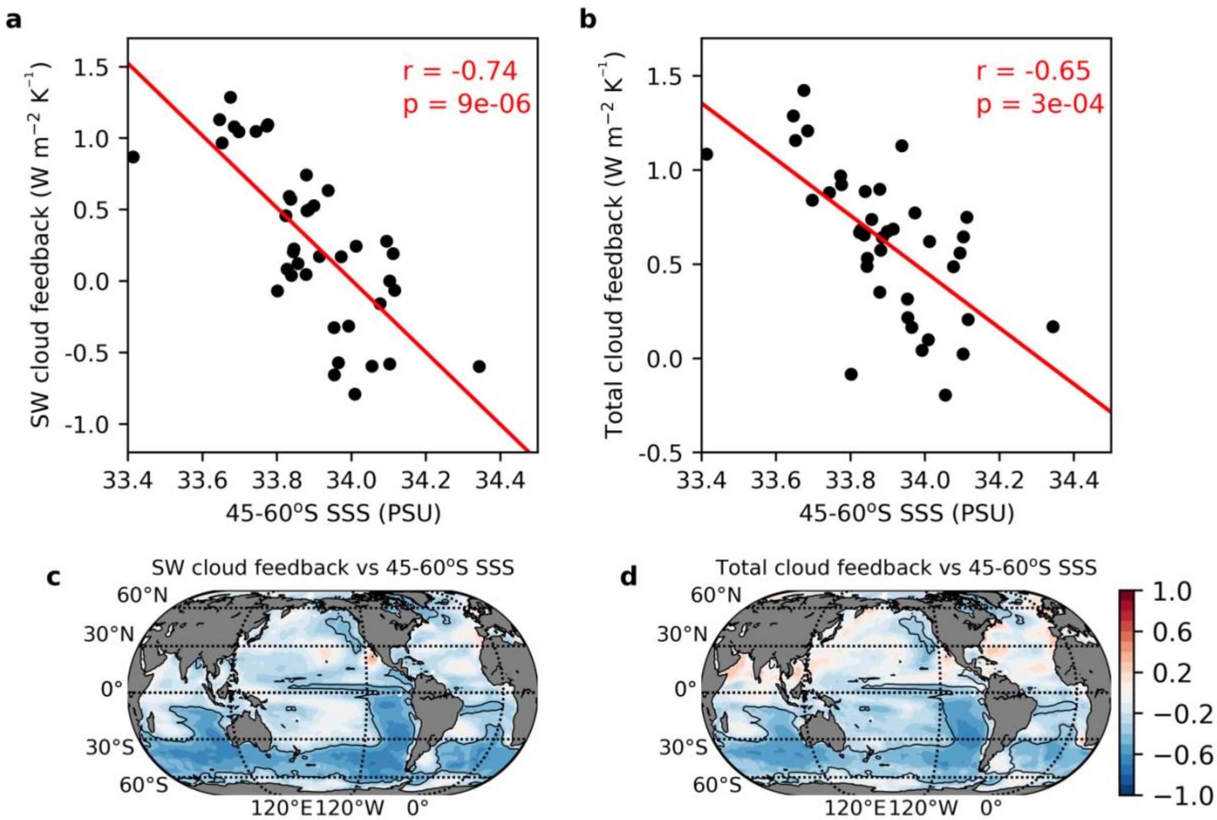

Figure 1. **The statistical link between extratropical Southern Ocean SSS and cloud feedback.** **a**, scatterplot of long-term global-mean SW cloud feedback from standard 150-year abrupt-4xCO2 experiments and base-state SSS averaged within the zone of 45º-60ºS from pre-industrial control experiments among 40 CMIP6 climate models (black dots). Pearson's correlation and corresponding p-value are indicated in red. The red line indicates the best-fit linear regression. **b**, same as **a**, but for long-term global-mean total cloud feedback. **c**, Pearson's correlation between 45º-60ºS SSS and the spatial pattern of long-term SW cloud feedback. Areas with significance level less than 0.05 are indicated with thin black lines. **d**, same as **c**, but for the spatial pattern of total cloud feedback.

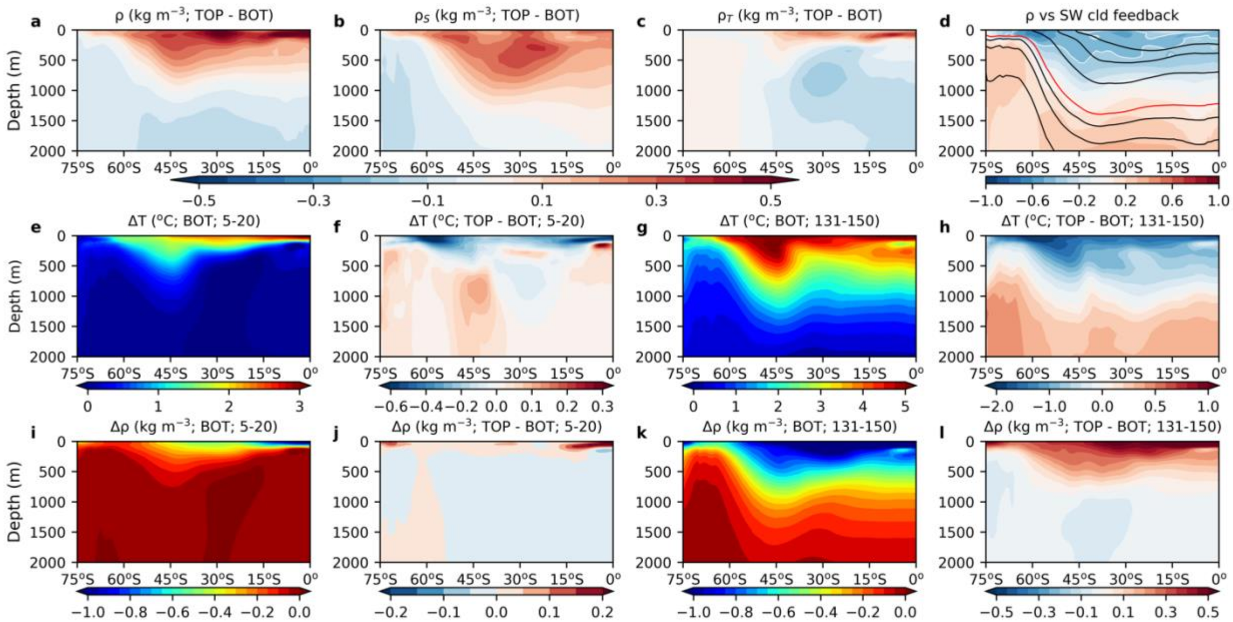

Figure 2. **Impact of base-state salinity on ocean temperature and density response.** **a**, the difference in zonal-mean base-state ocean density between top and bottom salinity models. **b**, **c** same as **a**, but for the contribution of ocean salinity and temperature to ocean density difference, respectively. **d**, Latitude-depth distribution of Pearson's correlation (shaded color) between zonal-mean ocean density and long-term global-mean SW cloud feedback. Areas with significance level of less than 0.05 are indicated with thin white lines. The potential density is indicated with black and red (for density of 1027.6 kg m^{-3}) lines. **e**, zonal-mean ocean temperature response from bottom salinity models. The response is computed as the difference between year 5–20 from the 150-year abrupt-4xCO2 experiment and year 1–100 from the pre-industrial control experiment. The first five years are excluded due to fast model adjustments. **f**, same as **e**, but for the difference in zonal-mean ocean temperature response between top and bottom models. **g**, **h**, same as **e**, **f**, but for model years 131-150 from the abrupt-4xCO2 experiment. **i-l**, same as **e-h**, but for ocean density response.

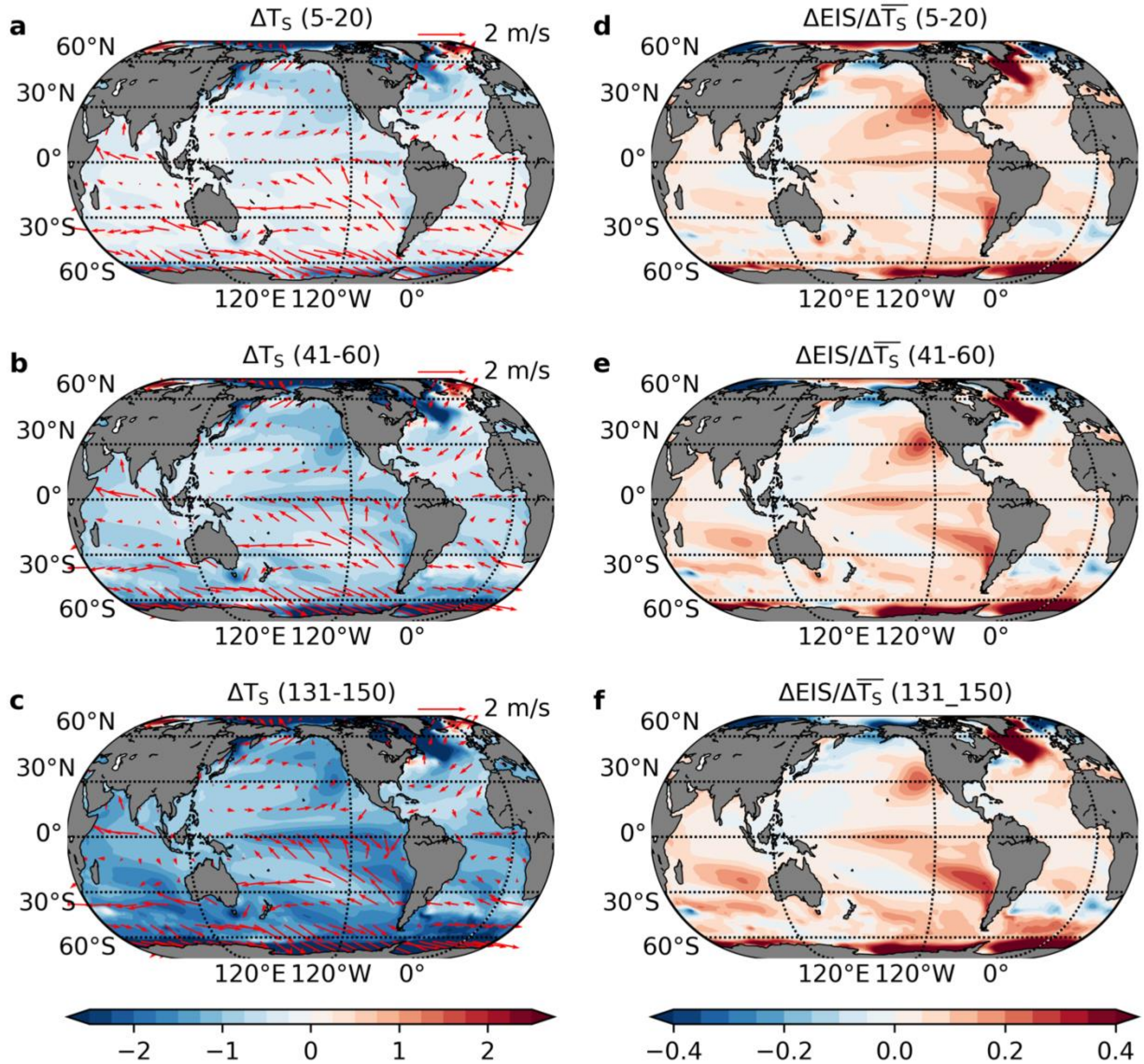

Figure 3. **Ocean salinity impact on responses of SST, surface wind, and estimated inversion strength to CO2 forcing. a**, difference in SST response (shaded color) between top and bottom salinity models and surface wind response (arrows) averaged from all models. The response is computed as the difference between year 5–20 from the 150-year abrupt-4xCO2 experiment and year 1–100 from the pre-industrial control experiment. **b**, **c**, same as **a**, but for model years of 41-60 and 131-150 from abrupt-4xCO2 experiment. **d-f**, same as **a-c**, but for 700-hPa estimated inversion strength response normalized by the global-mean surface temperature change.

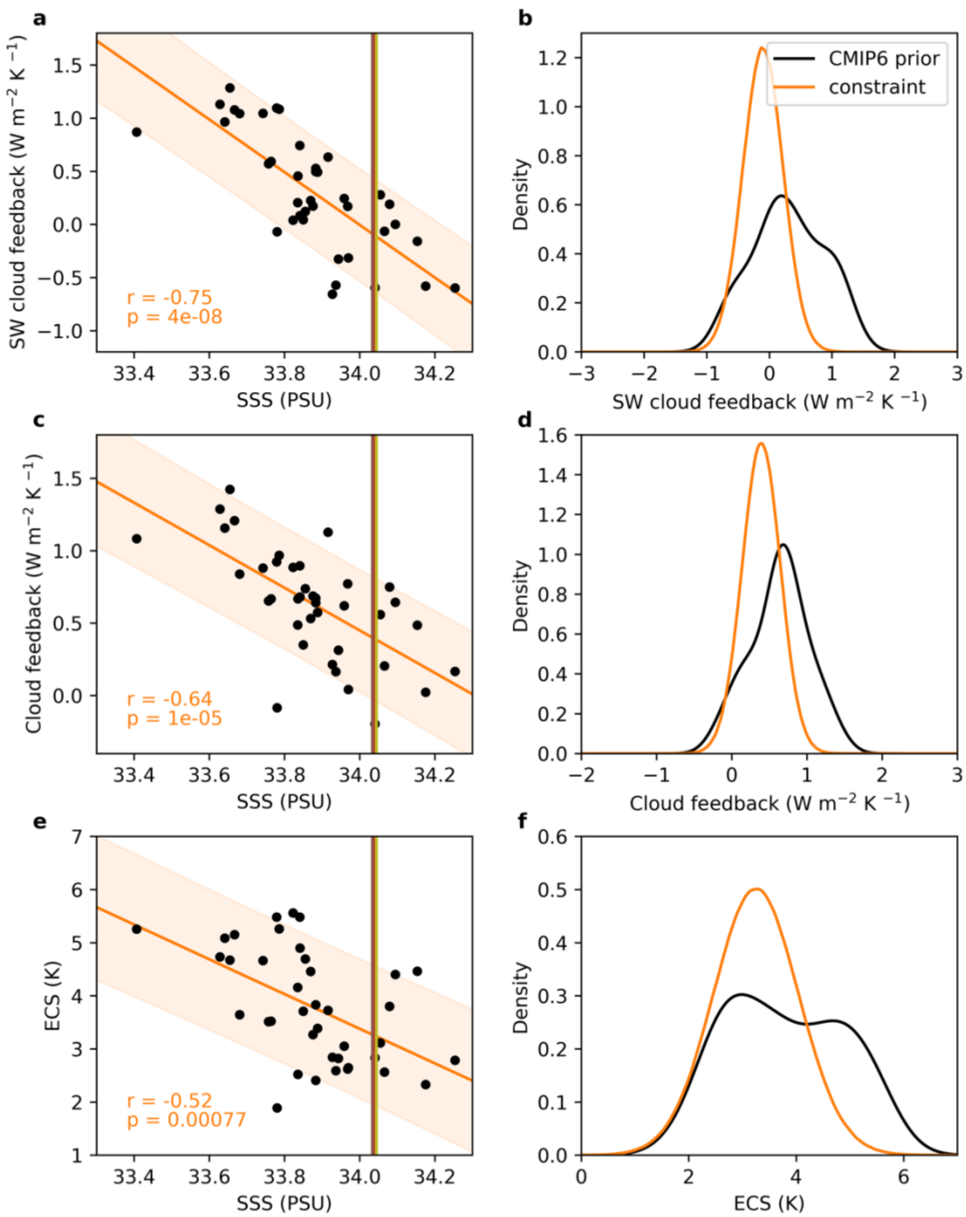

Figure 4. **Emergent constraint on cloud feedback and ECS.** **a**, the ordinary least squares regression of 45^{o}-60^{o}S SSS from the historical runs over the period of 1968-2014 and long-term global-mean SW cloud feedback from 150-year abrupt-4xCO2 experiment among 39 CMIP6 coupled climate models. GISS-E2-2-G model is excluded due to the lack of historical SSS variable. The orange line and shaded area indicate the linear regression fit and associated prediction level [5%, 95%], respectively. The three vertical lines denote 45^{o}-60^{o}S SSS over the period of 1968-2014 from the three observation-constrained salinity data sets (from left to right: Ishii, ORAS4, IAP). **b**, the probability density function of SW cloud feedback from CMIP6 models prior to emergent constraint (black) and after constraint (orange). The density function is estimated from Gaussian kernels. **c, d**, same as **a, b**, but for total cloud feedback. **e, f**, same as **a, b**, but for ECS.

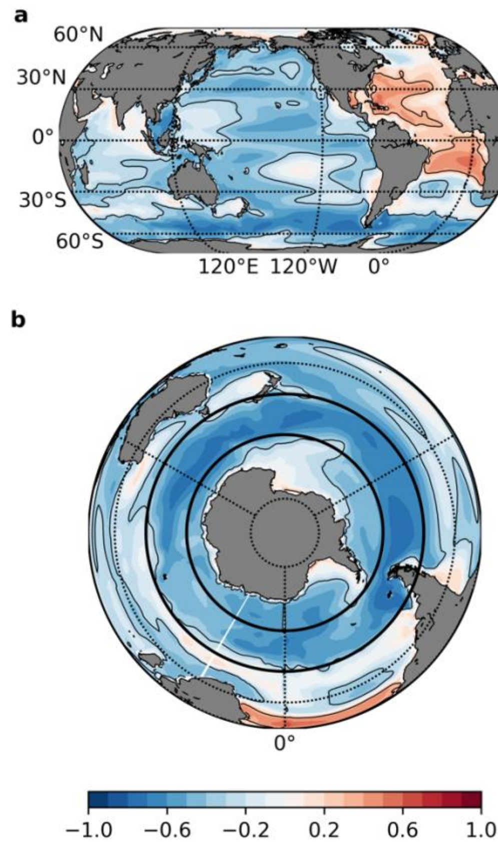

Extended Data Figure 1. **Statistical link between cloud feedback and extratropical Southern Ocean SSS. a**, the Pearson's correlation between long-term global-mean SW cloud feedback and the spatial pattern of base-state SSS from the 40 CMIP6 coupled climate models. Areas with significance level less than 0.05 are indicated with thin black lines. **b**, same as **a**, but based on orthographic projection. The zonal ring between 45º-60ºS is indicated by the two thick black lines.

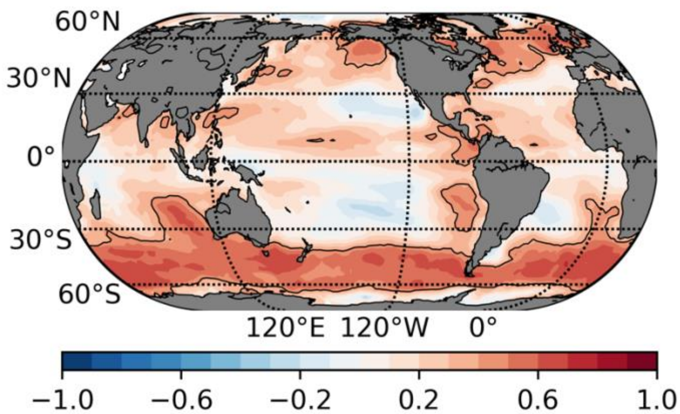

Extended Data Figure 2. **Pearson correlation between 45º-60ºS SSS and long-term longwave cloud feedback**. Areas with significance level of at least 0.05 are indicated with thin black lines.

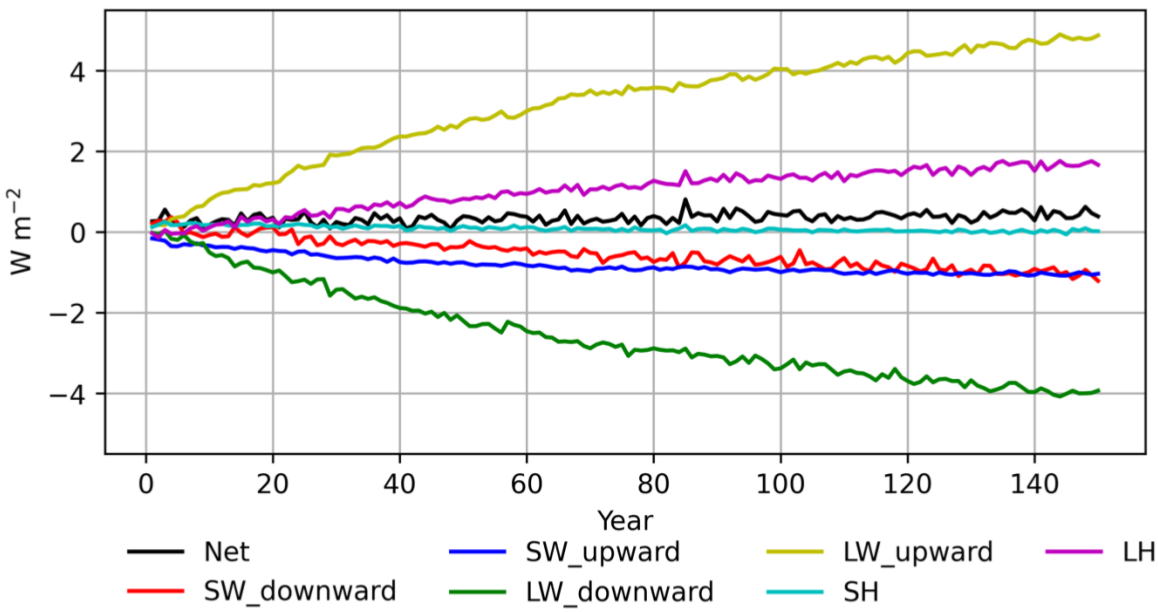

Extended Data Figure 3. **Surface energy flux analysis**. Time series of difference in annual net surface energy flux response to CO_2 forcing between top and bottom salinity models and the contribution from all components. The fluxes are computed as the latitude-weighted mean for regions south of 35ºS.

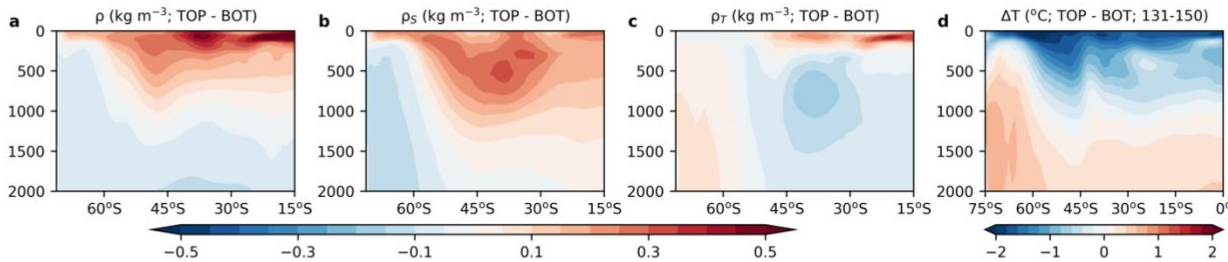

Extended Data Figure 4. **Impact of lower MOC on ocean temperature response.** **a**, the difference in zonal-mean base-state ocean density between top and bottom models. The top and bottom models are selected based on the response of lower MOC strength to CO2 forcing. **b**, **c** same as **a**, but for the contribution of ocean salinity and temperature to ocean density difference, respectively. **d**, the difference in zonal-mean ocean temperature response between top and bottom models. The response is computed as the difference between year 131–150 from the 150-year abrupt-4xCO2 experiment and year 1–100 from the pre-industrial control experiment.

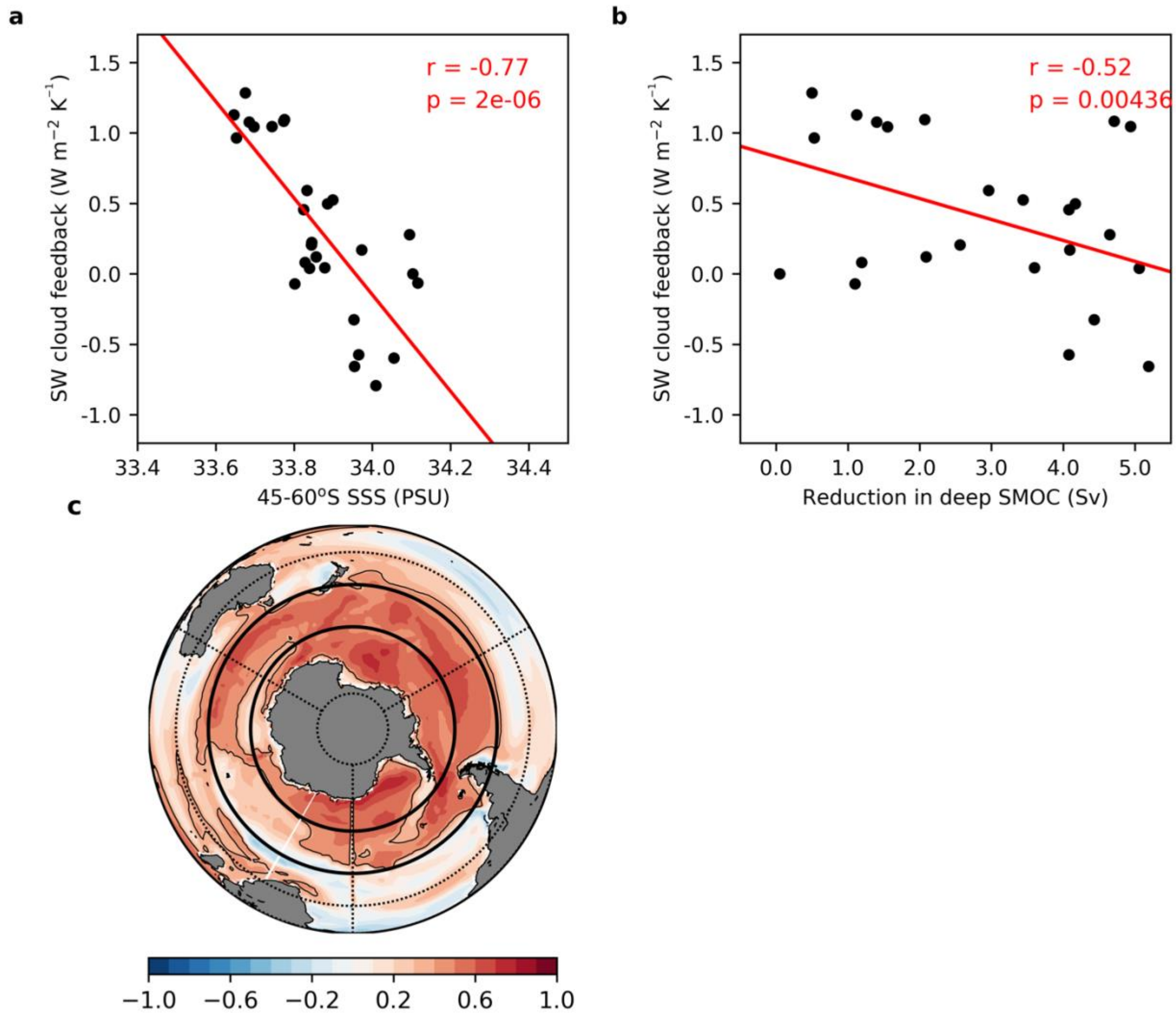

Extended Data Figure 5. **Comparison of the impact of extratropical Southern Ocean SSS and lower MOC response on SW cloud feedback. a**, scatterplot of long-term global-mean SW cloud feedback from standard 150-year abrupt-4xCO2 experiments and base-state SSS averaged within the zone of 45°-60°S from pre-industrial control experiments among 25 CMIP6 climate models (black dots) with MOC data available. Pearson's correlation and corresponding p-value areindicated in red. The red line indicates the best-fit linear regression. **b**, same as **a**, but for the response of lower MOC to CO2 forcing. **c**, the spatial pattern of Pearson's correlation between lower MOC response and spatial SSS. The two black lines indicate the latitude of 45°S and 60°S, respectively.

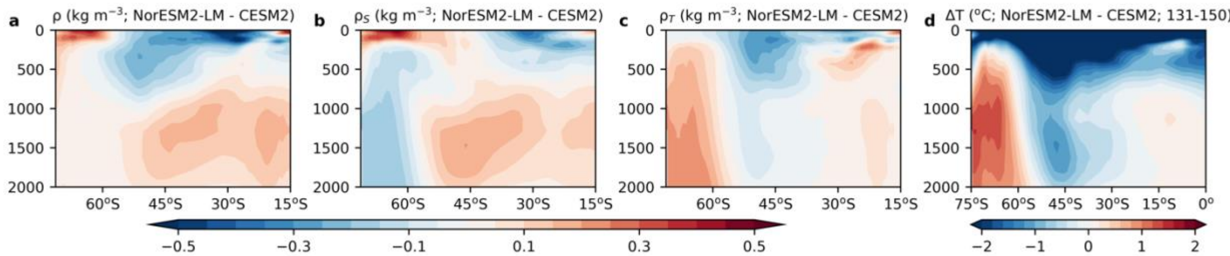

Extended Data Figure 6. **Comparison between NorESM2-LM and CESM2 model. a-d**, same as Extended Data Figure 4, but for the difference between NorESM2-LM and CESM2 instead of top and bottom models.

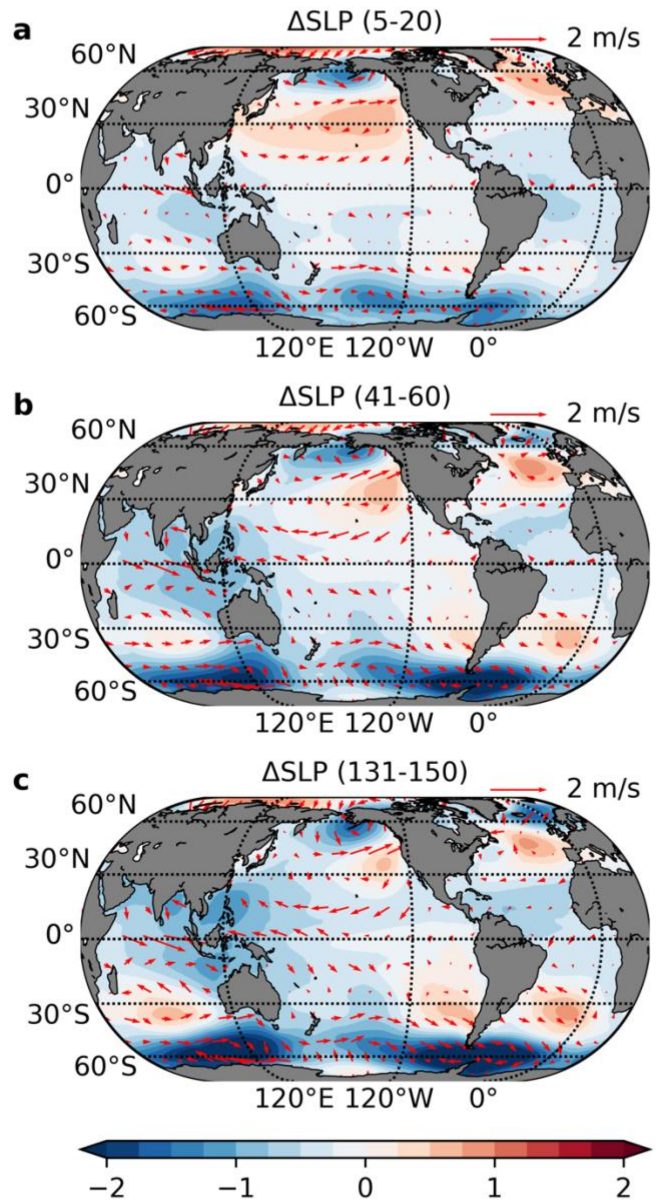

Extended Data Figure 7. **Ocean salinity impact on responses of sea level pressure and surface winds to CO2 forcing. a**, difference in sea level pressure (shaded color) and surface wind (arrows) response between top and bottom salinity models. The response is computed as the difference between year 5–20 from the 150-year abrupt-4xCO2 experiment and year 1–100 from the pre-industrial control experiment. **b**, **c**, same as **a**, but for model years of 41-60 and 131-150 from abrupt-4xCO2 experiment.

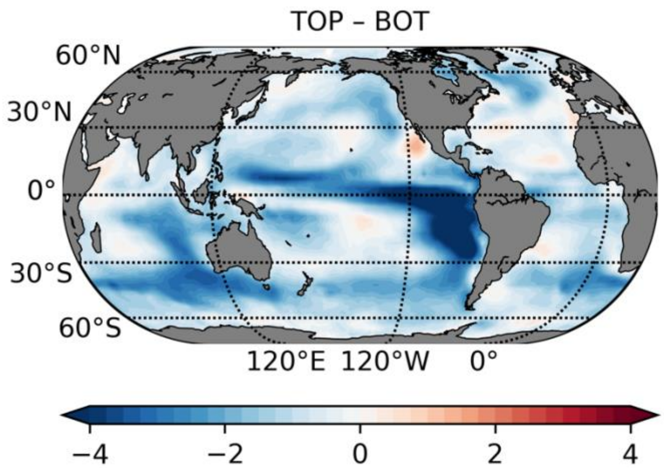

Extended Data Figure 8. **Impact of ocean salinity on the response of SW cloud feedback to CO2 forcing**. Difference in long-term SW cloud feedback between top and bottom salinity models.

Extended Data Table 1. The 40 CMIP6 coupled climate models used in this study. 45°S-60°S SSS, long-term global-mean SW and total cloud feedback in response to abrupt CO_2 quadrupling, ECS and reduction in lower MOC are shown in values. Models with (without) available data for surface energy flux, ocean analyses (except MOC), and surface wind are indicated with “Y” (“N”).

No.	Model	45°-60°S SSS (PSU)	SW cloud feedback (W m^{-2} K^{-1})	Cloud feedback (W m^{-2} K^{-1})	ECS (K)	Reduction in lower MOC (Sv)	Surface energy flux	Ocean analysis	Surface wind
1	ACCESS-CM2	33.74	1.05	0.88	4.66	4.94	Y	Y	Y
2	ACCESS-ESM1-5	33.90	0.53	0.67	3.83	3.44	Y	Y	Y
3	BCC-CSM2-MR	34.01	0.24	0.62	3.05	N	Y	Y	Y
4	BCC-ESM1	33.91	0.17	0.69	3.27	N	Y	Y	Y
5	CanESM5	33.84	0.04	0.89	5.56	5.06	Y	Y	Y
6	CAS-ESM2-0	33.88	0.49	0.57	3.39	N	Y	Y	Y
7	CESM2	33.65	0.97	1.16	5.09	0.53	Y	Y	N
8	CESM2-FV2	33.69	1.08	1.21	5.15	1.40	Y	Y	N
9	CESM2-WACCM	33.68	1.29	1.42	4.67	0.50	Y	Y	N
10	CESM2-WACCM-FV2	33.65	1.13	1.29	4.73	1.12	Y	Y	N
11	CIESM	33.88	0.74	0.90	5.48	N	N	Y	N
12	CMCC-CM2-SR5	33.83	0.59	0.67	3.52	2.96	Y	Y	Y
13	CMCC-ESM2	33.84	0.57	0.65	3.52	N	Y	Y	Y
14	CNRM-CM6-1	33.83	0.08	0.68	4.90	1.19	Y	Y	Y
15	CNRM-CM6-1-HR	34.10	0.00	0.64	4.40	0.05	Y	N	Y
16	CNRM-ESM2-1	33.86	0.12	0.74	4.69	2.09	Y	Y	Y
17	E3SM-1-0	33.41	0.87	1.08	5.25	N	Y	Y	N
18	EC-Earth3-AerChem	33.88	0.04	0.35	3.71	3.60	Y	Y	Y
19	EC-Earth3-Veg	33.84	0.21	0.49	4.16	2.56	Y	Y	Y
20	FGOALS-g3	34.34	-0.60	0.17	2.78	N	Y	N	N
21	GFDL-CM4	34.11	0.19	0.75	3.80	N	Y	Y	Y
22	GFDL-ESM4	33.97	0.17	0.77	2.62	4.09	Y	Y	Y
23	GISS-E2-1-G	33.96	-0.57	0.16	2.59	4.08	Y	Y	Y
24	GISS-E2-2-G	34.01	-0.79	0.10	2.28	7.87	Y	Y	Y
25	HadGEM3-GC31-LL	33.78	1.10	0.92	5.48	2.07	Y	Y	Y
26	IITM-ESM	34.10	-0.58	0.02	2.33	N	Y	N	Y
27	INM-CM5-0	33.80	-0.07	-0.08	1.89	1.1	Y	N	Y
28	IPSL-CM5A2-INCA	33.94	0.63	1.13	3.73	N	N	Y	Y
29	IPSL-CM6A-LR	33.85	0.22	0.53	4.46	5.58	Y	Y	Y
30	MIROC6	34.12	-0.06	0.21	2.57	8.12	Y	Y	Y
31	MIROC-ES2L	33.99	-0.32	0.04	2.65	N	Y	N	Y

32	MPI-ESM-1-2-HAM	34.06	-0.60	-0.20	2.83	5.83	Y	Y	Y
33	MPI-ESM1-2-HR	33.95	-0.33	0.31	2.82	4.43	Y	Y	Y
34	MPI-ESM1-2-LR	33.95	-0.66	0.21	2.84	5.19	Y	Y	Y
35	MRI-ESM2-0	34.09	0.28	0.56	3.11	4.65	Y	Y	Y
36	NESM3	34.08	-0.16	0.49	4.46	N	Y	Y	N
37	NorESM2-LM	33.82	0.46	0.67	2.52	4.08	Y	Y	N
38	NorESM2-MM	33.89	0.50	0.64	2.41	4.17	Y	Y	N
39	SAM0-UNICON	33.70	1.04	0.84	3.64	1.55	Y	Y	N
40	UKESM1-0-LL	33.77	1.08	0.97	5.26	4.71	Y	N	Y